Structure of the DMPC lipid bilayer ripple phase: Supporting Information

Kiyotaka Akabori and John F. Nagle

Department of Physics, Carnegie Mellon University
Pittsburgh, PA, 15213 (USA)

Contents

List of Tables

List of Figures

Additional content may also be found in the Ph.D. thesis of Kiyotaka Akabori that can be accessed at http://lipid.phys.cmu.edu.

S1 Sample q-space

The incoming and outgoing wavevectors of the X-ray beam in Fig. 1 are given by

$$\mathbf{k}_{\text{in}} = \frac{2\pi}{\lambda}\hat{\mathbf{y}}, \quad \mathbf{k}_{\text{out}} = \frac{2\pi}{\lambda}\left(\sin 2\theta\cos\phi\,\hat{\mathbf{x}} + \cos 2\theta\,\hat{\mathbf{y}} + \sin 2\theta\sin\phi\,\hat{\mathbf{z}}\right), \tag{1}$$

where λ is the X-ray wavelength, 2θ is the total scattering angle, and ϕ is the angle measured from the equator on the detector. The scattering vector (also called momentum transfer vector) is the difference between $\mathbf{k}_{\text{out}}$ and $\mathbf{k}_{\text{in}}$,

$$\begin{aligned}\mathbf{q} &= \mathbf{k}_{\text{out}} - \mathbf{k}_{\text{in}} \\ &= q\left(\cos\theta\cos\phi\,\hat{\mathbf{x}} - \sin\theta\,\hat{\mathbf{y}} + \cos\theta\sin\phi\,\hat{\mathbf{z}}\right),\end{aligned} \tag{2}$$

where $q = 4\pi\sin\theta/\lambda$ is the magnitude of the scattering vector. When the sample is rotated by ω about the lab x-axis in the clockwise direction as shown in Fig. 1, the sample q-space also rotates and is given by

$$\hat{\mathbf{e}}_{\mathbf{x}} = \hat{\mathbf{x}}, \quad \hat{\mathbf{e}}_{\mathbf{y}} = \cos\omega\,\hat{\mathbf{y}} + \sin\omega\,\hat{\mathbf{z}}, \quad \hat{\mathbf{e}}_{\mathbf{z}} = -\sin\omega\,\hat{\mathbf{y}} + \cos\omega\,\hat{\mathbf{z}}. \tag{3}$$

From Eq. (2) and (3), we find Cartesian components of the sample q-space to be

$$\begin{aligned}q_x &= \mathbf{q}\cdot\hat{\mathbf{e}}_{\mathbf{x}} = q\cos\theta\cos\phi, \\ q_y &= \mathbf{q}\cdot\hat{\mathbf{e}}_{\mathbf{y}} = q\left(-\sin\theta\cos\omega + \cos\theta\sin\phi\sin\omega\right), \\ q_z &= \mathbf{q}\cdot\hat{\mathbf{e}}_{\mathbf{z}} = q\left(\sin\theta\sin\omega + \cos\theta\sin\phi\cos\omega\right).\end{aligned} \tag{4}$$

The position, (X,Z), of a CCD pixel is measured with respect to the beam and given by

$$X = S\tan 2\theta\cos\phi, \quad Z = S\tan 2\theta\sin\phi, \tag{5}$$

where S is the distance between the sample and detector. From a model for the electron density of a lipid bilayer, one calculates the X-ray scattering intensity pattern, $I(\mathbf{q})$. Then, Eq. (4) and (5) relate $I(\mathbf{q})$ to the experimentally measured intensity pattern, $I(X,Z)$.

For low angle X-ray scattering (LAXS), it is convenient to linearize Eq. (4) in terms of θ and ω. In the small angle approximation, $\sin\phi \approx Z/(2S\theta)$ and

$\cos\phi \approx X/(2S\theta)$, and

$$
\begin{aligned}
q_x &\approx \frac{4\pi\theta\cos\phi}{\lambda} \approx kX/S \\
q_y &\approx q_z\omega - \frac{4\pi\theta^2}{\lambda} \approx q_z\omega - \frac{\lambda q_z^2}{4\pi} \\
q_z &\approx \frac{4\pi\theta\sin\phi}{\lambda} \approx kZ/S,
\end{aligned} \tag{6}
$$

with $k = 2\pi/\lambda$. For wide angle X-ray scattering, the exact relations given by Eq. (4) are necessary. Especially in the transmission experiment, where ω is large, an observed X-ray pattern appears nontrivial, and quantitative analysis requires Eq. (4).

S2 LAXS Data Reduction

The lattice structure of a stack of bilayers in the ripple phase is a two dimensional monoclinic lattice. In an oriented sample, the stacking z direction and the ripple x direction are separated, rendering peak indexing a trivial task as shown in the next subsection. However, obtaining the form factors from measured intensity is considerably more involved and requires the development of the three correction factors described in the following three subsections.

S2.1 Lattice Structure – Unit Cell

The unit cell vectors for the two-dimensional oblique lattice shown in Fig. S1 can be expressed as[4]

$$\mathbf{a_1} = \frac{D}{\tan\gamma}\hat{\mathbf{x}} + D\hat{\mathbf{z}} \tag{7}$$

and

$$\mathbf{a_2} = \lambda_r\hat{\mathbf{x}}. \tag{8}$$

The corresponding reciprocal lattice unit cell vectors are

$$\mathbf{A_1} = \frac{2\pi}{D}\hat{\mathbf{z}} \tag{9}$$

and

$$\mathbf{A_2} = \frac{2\pi}{\lambda_r}\hat{\mathbf{x}} - \frac{2\pi}{\lambda_r\tan\gamma}\hat{\mathbf{z}}. \tag{10}$$

The reciprocal lattice vector, $\mathbf{q}_{hk}$ for the Bragg peak with Miller indices (h,k) is

$$\mathbf{q}_{hk} = h\mathbf{A_1} + k\mathbf{A_2}, \tag{11}$$

so its Cartesian components are

$$\mathbf{q}_{hk} \cdot \hat{\mathbf{x}} = q^x_{hk} = \frac{2\pi k}{\lambda_r} \tag{12}$$

$$\mathbf{q}_{hk} \cdot \hat{\mathbf{y}} = q^y_{hk} = 0 \tag{13}$$

$$\mathbf{q}_{hk} \cdot \hat{\mathbf{z}} = q^z_{hk} = \frac{2\pi h}{D} - \frac{2\pi k}{\lambda_r \tan\gamma}. \tag{14}$$

Our sample consists of many ripple domains with a uniform distribution of in-plane directions of the ripple wavevector, $\mathbf{a_2}$ in Fig. S1. This means that, for any (h,k) reflection, there is always a domain that has an in-plane orientation such that quasi-elastic scattering occurs and a peak is observed on the CCD. In this case, q^x_{hk} and q^y_{hk} may be combined to give $q^r_{hk} = 2\pi k/\lambda_r$. Fig. 2 shows this Miller index pattern from which the in-plane ripple repeat distance λ_r = 145.0 Å, the out-of-plane repeat distance D = 57.8 Å, and the oblique angle $\gamma = 98.2°$ for that sample were easily obtained. Values of q^r_{hk} and q^z_{hk} for observed reflections are included in Tables S3 and S4.

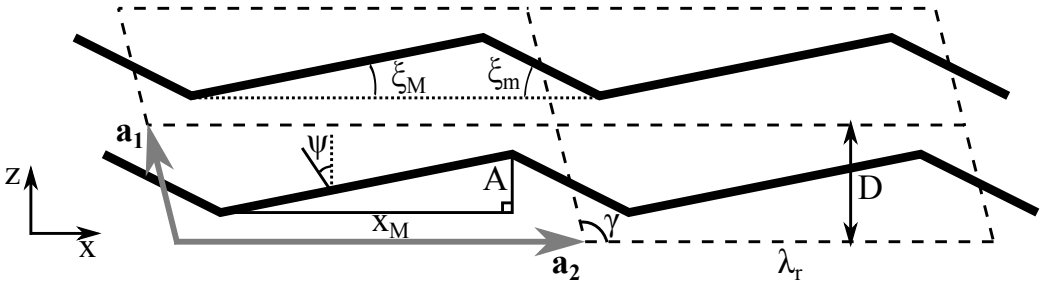

Fig. S1 Unit cells for the lattice are shown by dashed lines. The schematic for the bilayer centers is shown by thick, solid lines. Notations in the figure are ($\mathbf{a_1}$ and $\mathbf{a_2}$: lattice unit vectors), (D: lamellar repeat distance along z), ($\lambda_r = |\mathbf{a_2}|$: ripple wavelength), ($\gamma$: oblique angle), ($A$: ripple amplitude), ($\psi$: chain tilt angle with respect to the z-axis), and (x_{M}: projected length of the major arm).

S2.2 Lorentz Correction

Our sample has in-plane rotational symmetry about the z-axis. Ignoring mosaic spread to which we will come back later, this means that the sample consists

of many domains with differing ripple directions, assuming that all domains are parallel to the substrate. In sample q-space, ripple $(h,k \neq 0)$ side peaks are represented as rings centered at the meridian, or q_z-axis, while $(h,k=0)$ main peaks are still points on the meridian (see Fig. S2). Then, for an arbitrary incident angle ω, $(h,0)$ peaks are not observed while side peaks are observed for a range of ω as will now be explained.

In order to capture all (h,k) peaks in one X-ray exposure, the sample was continuously rotated over a range of ω, $\Delta\omega$, about the x-axis. As a result of this rotation, the $(h,0)$ main peaks become arcs that subtend an angle $\Delta\omega$, as shown in Fig. S3, with its lengths equal to $\Delta\omega q_{h0}^z$. The detector records the intersections of these arcs with the Ewald sphere, so the intrinsic scattering intensity of the $(h,0)$ reflections is the product of the observed intensity, I_{h0}^{obs} with the arc length, that is,

$$I_{h0} = \Delta\omega q_{h0}^z I_{h0}^{\text{obs}}. \tag{15}$$

This gives the usual Lorentz correction for lamellar orders.

Now, we consider relative intensity of side peaks for a given order h. As described earlier, $(h,k \neq 0)$ side peaks are represented as rings whose radius is q_{hk}^r in the sample q-space. Because only the domains with the right ripple direction can satisfy Bragg's condition at a given fixed angle ω, the intrinsic scattering intensity in this ring is reduced by a factor of $2\pi q_k^r$ compared to the $(h,0)$ reflections. This reduction of intensity can be nicely visualized by the Ewald sphere construction shown in Fig. S2, which shows that entire rings are not intersected by the Ewald sphere at a fixed angle. Then, the intrinsic scattering intensity in a ring is

$$I_{hk\neq 0} \propto 2\pi q_{hk}^r I_{hk}^{\text{obs}}. \tag{16}$$

During an X-ray exposure, the sample q-space rotates and the rings are intersected by the Ewald sphere at all our experimental incident angles ω. However, as Fig. S4 shows, only small parts of the rings are actually intersected with the Ewald sphere. To obtain the full expression for $(h,k \neq 0)$ reflections, we now turn to a more rigorous calculation.

Mathematically, the rotation is equivalent to an integration over ω. In LAXS, q_z is nearly constant at a given pixel as ω is varied, which can be seen from Eq. (6). As Eq. (6) shows, ω dependence appears only through q_y, so rotating the sample is realized by integrating over q_y; formally, we write $d\omega = dq_y/q_z$. To derive the integration limits on q_y, let us consider two cases: (1) When $\omega \leq 0$, the incoming X-ray beam is blocked by the back of the substrate. This sets the lower limit of ω to 0. Plugging $\omega = 0$ in Eq. 6), we find the lower limit of the q_y integration

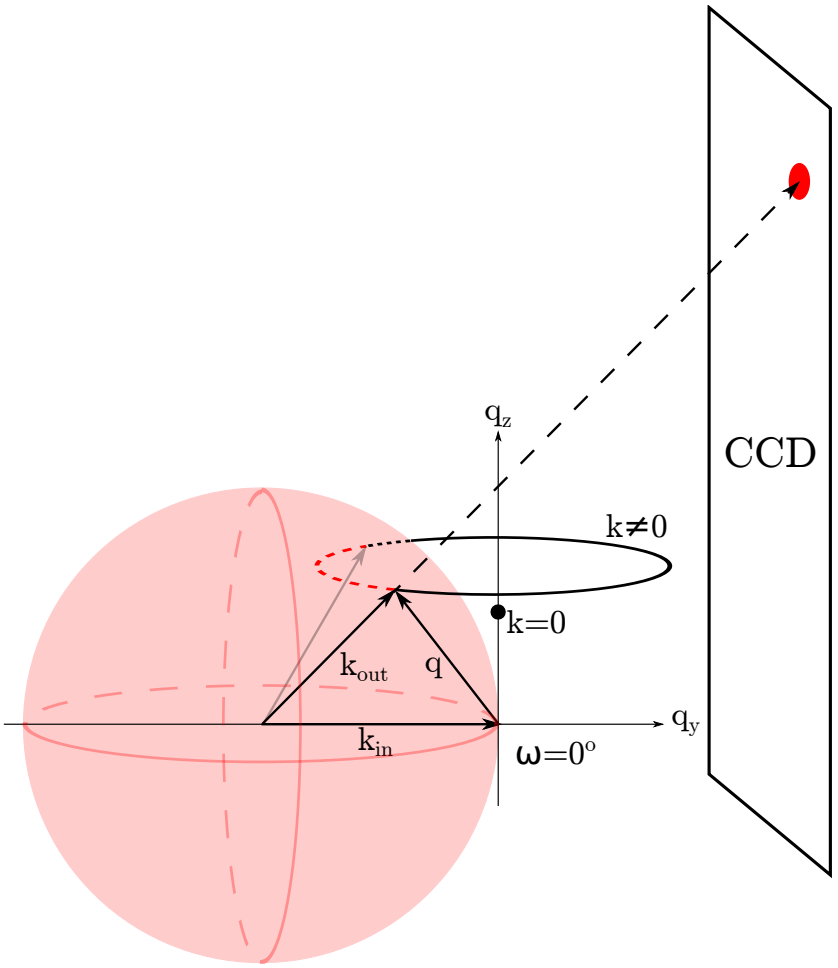

Fig. S2 Ewald sphere construction to obtain relation between location of scattering peaks on the CCD and their q-space values. The incoming X-ray wavevector is $\mathbf{k}_{\text{in}}$, and $\mathbf{k}_{\text{out}}$ is a scattered X-ray wavevector with $|\mathbf{k}_{\text{out}}| = |\mathbf{k}_{\text{in}}|$ for the predominant quasi-elastic scattering. A part of the q-space pattern is shown for the ripple phase in the low angle regime. For $(h,k=0)$ Miller indices, there are points labelled $k=0$ on the q_z axis. For $(h,k\neq 0)$ there are rings labelled $k\neq 0$ centered on the q_z-axis. The red dashed line shows the portion of a ring that is inside the Ewald sphere and the portion outside is shown as a black solid or dashed line. Diffraction occurs where the ring and the sphere intersect. For our wavelength of 1.175 Å, $|\mathbf{k}_{\text{in}}| = 5.35$ Å^{-1} and for $h=5$, $q_{50}^z = 0.54$ Å^{-1}, one tenth of $|\mathbf{k}_{\text{in}}|$. For clarity $|\mathbf{q}|$ is drawn large compared to $|\mathbf{k}_{\text{in}}|$.

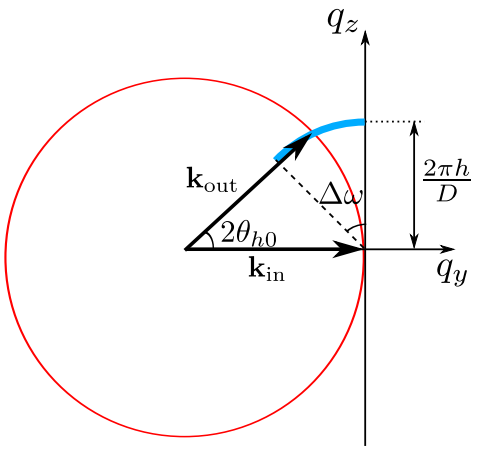

Fig. S3 Trajectory of $k = 0$ peak as the sample is rotated by ω is shown as a thick blue line.

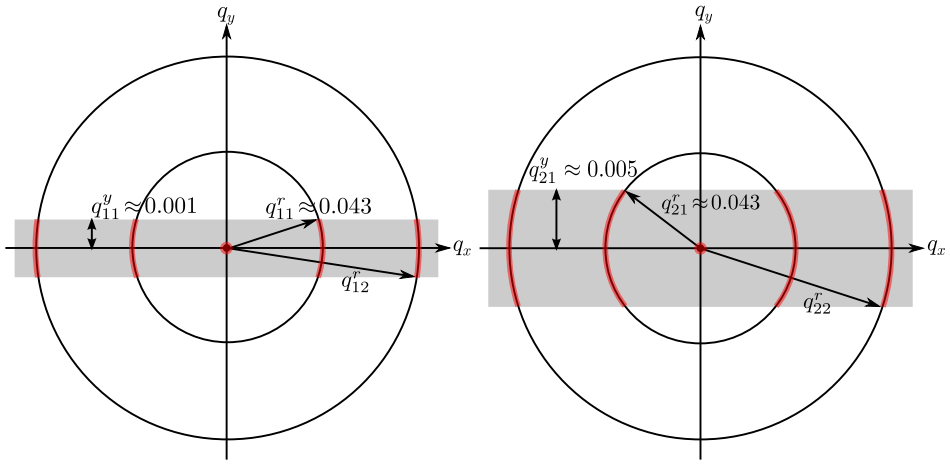

Fig. S4 q-space representations of Bragg peaks and Bragg rings for h = 1 and 2 and k = 0, 1, and 2 in q_{hk}^z planes. The intersection between the Ewald sphere and a Bragg peak/ring is indicated in red. The observed intensity for the $k \neq 0$ orders is proportional to the fraction of the length of red arcs to the circumference. This fraction is equal to one for $k = 0$ reflections. Because the reflections are not in the same q_z plane, the range of q_y integration indicated by the height of the gray rectangle is different for different h orders. For $\gamma \neq 90°$, the range of q_y integration is slightly different for different k reflections with the same h. The values shown are for $D = 58$ Å, $\lambda_r = 145$ Å, $\gamma = 90°$, and $\lambda = 1.175$ Å. For visibility, the height of the gray rectangles is exaggerated by about a factor of 10, exaggerating the arc curvature. With the shown large curvature, the peaks would have an asymmetric shape in the q_r direction.

to be $-\lambda q_z^2/(4\pi)$. (2) When $\omega \geq 2\theta$, the substrate blocks the outgoing X-ray, so the maximum $\omega = 2\theta$. Within the small angle approximation, $q_z \approx 4\pi\theta/\lambda$. Then, the maximum ω can be expressed as $\lambda q_z/(2\pi)$. Plugging this expression for ω in Eq. (6), we find the upper limit of the q_y integration to be $\lambda q_z^2/(4\pi)$. Also integrating over the detector pixels X and Z to obtain integrated intensity, we write the observed intensity as

$$\begin{aligned} I_{hk}^{\text{obs}} &\propto \int dX \int dZ \int d\omega\, I_{hk} \\ &\propto \int dq_x \int dq_z \int_{-\frac{\lambda q_z^2}{4\pi}}^{\frac{\lambda q_z^2}{4\pi}} \frac{dq_y}{q_z} I_{hk}(\mathbf{q}), \end{aligned} \tag{17}$$

where $1/q_z$ factor in q_y integration is the usual Lorentz polarization factor in the small angle approximation.

For a crystalline sample with in-plane rotational symmetry, the structure factor of a ripple Bragg peak is

$$S_{hk}(\mathbf{q}) = S_{hk}(q_r, q_z) = \frac{1}{2\pi q_r} \delta(q_r - q_{hk}^r)\delta(q_z - q_{hk}^z), \tag{18}$$

where $q_{hk}^r = 2\pi|k|/\lambda_r$. Thus, the scattering pattern in the ripple phase is a collection of Bragg rings for $k \neq 0$ centered at the meridian and the Bragg peaks for $k = 0$ located along the meridian. The scattering intensity is $I(\mathbf{q}) = |F(\mathbf{q})|^2 S(\mathbf{q})$, where $F(\mathbf{q})$ is the form factor. After the q_z integration, the observed, integrated intensity of (h,k) peak is proportional to

$$I_{hk}^{\text{obs}} \propto \frac{|F_{hk}|^2}{q_{hk}^z} \int dq_x \int_{-q_{hk}^{y0}}^{q_{hk}^{y0}} dq_y \frac{\delta(q_r - q_{hk}^r)}{2\pi q_r}, \tag{19}$$

where $q_{hk}^{y0} = \lambda (q_{hk}^z)^2/(4\pi)$. For side peaks ($k \neq 0$), we have

$$\begin{aligned} \int dq_x \int_{-q_{hk}^{y0}}^{q_{hk}^{y0}} dq_y \frac{\delta(q_r - q_{hk}^r)}{2\pi q_r} &\approx \int_{-q_{hk}^{y0}/q_{hk}^r}^{q_{hk}^{y0}/q_{hk}^r} d\phi \int dq_r\, q_r \frac{\delta(q_r - q_{hk}^r)}{2\pi q_r} \\ &= \frac{q_{hk}^{y0}}{\pi q_{hk}^r}. \end{aligned} \tag{20}$$

For main peaks ($k = 0$), we have

$$\begin{aligned} \int dq_x \int_{-q_{hk}^{y0}}^{q_{hk}^{y0}} dq_y \frac{\delta(q_r - q_{hk}^r)}{2\pi q_r} &= \int_0^{2\pi} d\phi \int dq_r\, q_r \frac{\delta(q_r - q_{hk}^r)}{2\pi q_r} \\ &= 1 \end{aligned} \tag{21}$$

Using Eq. (19 – 21), we write the observed integrated intensity as

$$I_{h0}^{\mathrm{obs}} \propto \frac{|F_{h0}|^2}{q_{h0}^z} \tag{22}$$

$$I_{hk}^{\mathrm{obs}} \propto \frac{|F_{hk}|^2}{q_{hk}^z}\frac{q_{hk}^{y0}}{\pi q_{hk}^r} = |F_{hk}|^2 \frac{\lambda q_{hk}^z}{2\pi}\frac{1}{2\pi q_{hk}^r} = |F_{hk}|^2 \frac{2\theta_{hk}}{2\pi q_{hk}^r}, \tag{23}$$

where $2\theta_{hk} = \lambda q_{hk}^z/(2\pi)$ is the incident angle at which the outgoing X-ray for the peak (h,k) is blocked by the substrate. Eq. (22) and (23) relate the form factor calculated from a model to the experimentally observed intensity.

S2.3 Absorption Correction for LAXS

In this subsection, we derive the absorption correction for an oriented sample. The calculation involves an explicit integration over the incident angle, ω, which is necessitated by the sample rotation during an X-ray exposure. The procedure is to write down an absorption factor, $A(\omega,\theta)$, for a given scattering angle 2θ at a given incident angle θ, and then integrate over ω. We ignore q_x dependence because the X-ray path inside the sample is nearly within the y-z plane for low angle scattering.

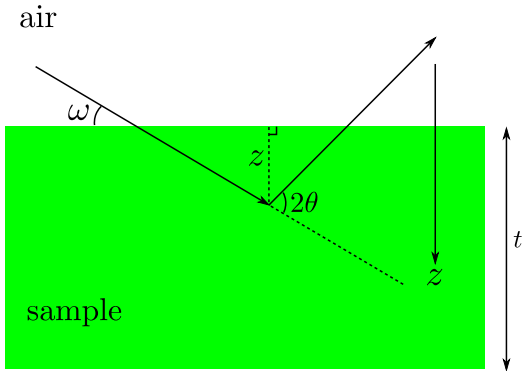

Fig. S5 The path of X-rays within the sample. The incident angle is ω and the total scattering angle is 2θ. An X-ray with a penetration depth of z is shown. The total thickness of the sample is t. Refraction correction is negligible for $\theta > 0.5°(h = 1)$.

Assume that all the X-rays enter the sample from the top surface. The total scattering angle is given by 2θ (see Fig. S5). Let the z-axis point downward. At

the top surface (air-sample interface), $z = 0$. For X-rays that travel to z and then scatter, the total path length within the sample is

$$L(z, \omega, \theta) = \frac{z}{\sin \omega} + \frac{z}{\sin(2\theta - \omega)} = z g(\omega, \theta), \tag{24}$$

where $g(\omega, \theta) = (\sin \omega)^{-1} + [\sin(2\theta - \omega)]^{-1}$. For each ray, the intensity is attenuated by the sample. Compared to the scattering intensity from $z = 0$, the attenuated intensity is

$$I(z, \omega, \theta) = I_0 \exp\left(-\frac{L}{\mu}\right), \tag{25}$$

where μ is the absorption length of an X-ray. μ is about 2.6 mm for 10.5 keV X-ray for both water and lipids in all phases[1]. The observed sample scattering intensity at fixed ω is equal to the integration of Eq. (25) over the total thickness of the sample and given by

$$\begin{aligned} I(\omega, \theta) &= \int_0^t dz I(z, \omega, \theta) = I_0 \int_0^t dz \exp\left(-\frac{g(\omega, \theta)}{\mu} z\right) \\ &= I_0 \mu \frac{1 - \exp\left(-\frac{t}{\mu} g(\omega, \theta)\right)}{g(\omega, \theta)}. \end{aligned} \tag{26}$$

Defining the absorption factor at a fixed angle to be $A(\omega, \theta)$, the observed intensity can also be written as

$$I(\omega, \theta) = A(\omega, \theta) t I_0, \tag{27}$$

where tI_0 is the intensity we would observe for non-absorbed X-rays. Equating Eq. (26) and (27), we get

$$A(\omega, \theta) = \frac{\mu}{t} \frac{1 - \exp\left(-\frac{t}{\mu} g(\omega, \theta)\right)}{g(\omega, \theta)}. \tag{28}$$

If μ is taken to infinity (no absorption), $A(\omega, \theta)$ goes to 1 as expected. The absorption factor A_{h0} for the $k = 0$ peaks is given by $A(\omega = \theta = \theta_B)$, plotted in Fig. S6. As shown, this factor is about 20 % for $h = 1$ peak relative to $h = 4$, so it is not negligible.

For $k \neq 0$ side peaks, an integration over the incident angle ω is necessary because these peaks are observable at all our experimental incident angles as described in section S2.2. The observed intensity for side peaks from a rotating sample is simply

$$I_{\text{obs}}(\theta) = \int_0^{2\theta} d\omega I(\omega, \theta). \tag{29}$$

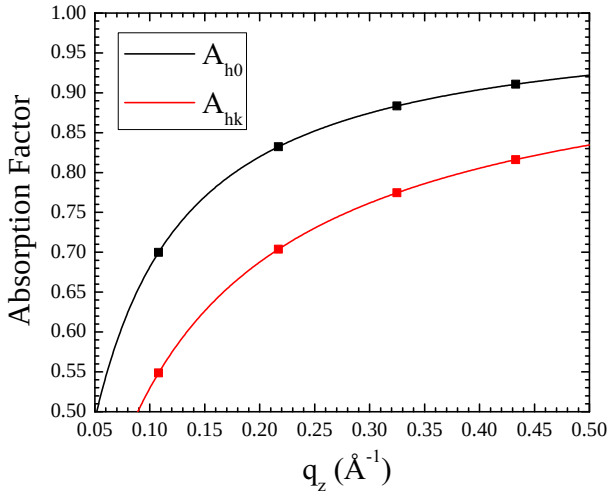

Fig. S6 Absorption factors Eq. (28) as a function of $q_z \approx 4\pi\theta/\lambda$. Values at $q_z = 2\pi h/D$ corresponding to $D = 57.8$ Å are shown as squares. μ = 2600 μm, t = 10 μm, and λ = 1.175 Å.

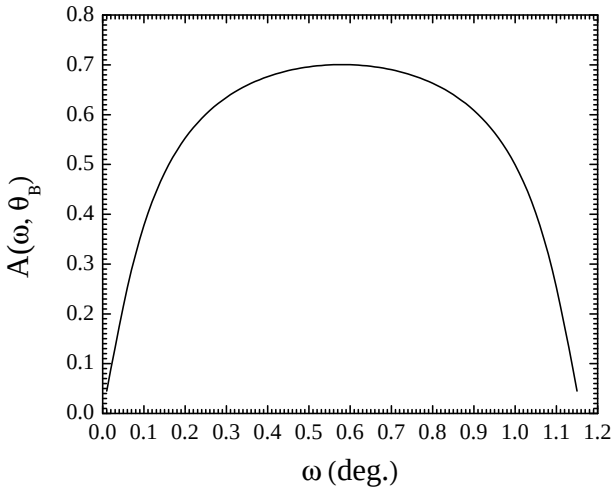

Fig. S7 Eq. (28) plotted as a function of ω for $\theta = \theta_B = 0.58°$, corresponding to the $h = 1$ Bragg angle for D = 57.8 Å.

The upper integration limit is equal to 2θ because the substrate completely blocks the scattered X-rays above this angle as discussed in section S2.2. Eq. (28), which is essentially the integrand in Eq. (29), is plotted in Fig. S7. It is maximum when $\omega = \theta$, meaning that the path length is shortest at the Bragg condition. The non-attenuated observed intensity is equal to $2\theta t I_0$. We define the absorption factor $A(\theta)$ to be the ratio of the total observed intensity to the total non-attenuated intensity,

$$A(\theta) \equiv \frac{I_{\text{obs}}(\theta)}{2\theta t I_0}. \tag{30}$$

Using Eq. (28) and (29) in (30), we arrive at the final absorption factor

$$A(\theta) = \frac{1}{2\theta}\int_0^{2\theta} d\omega A(\omega,\theta) = \frac{\mu}{2\theta t}\int_0^{2\theta} d\omega \frac{1-\exp\left(-\frac{t}{\mu}g(\omega,\theta)\right)}{g(\omega,\theta)}. \tag{31}$$

$A_{hk} = A(\theta)$ is plotted in Fig. S6. The absorption correction $A_c(\theta)$ is the inverse of Eq. (31).

S2.4 Correction due to Mosaic Spread

Integrated intensity needs to be corrected for mosaic spread, which consists of a distribution of domains of bilayers misoriented with respect to the substrate. During an X-ray exposure, the sample was continuously rotated. Due to this rotation, each pixel integrates intensity over a range of incident angles ω. A mosaic spread distribution can be probed by changing ω, so rotating the sample is essentially equivalent to integrating a mosaic spread distribution. Because the range of the distribution probed is approximately given by $\omega = [0, 2\theta_{hk}]$ where θ_{hk} is the Bragg angle for a (h,k) reflection, this range is larger for higher h orders. This effect is illustrated in Fig. S8.

We limit $\chi - \chi_{hk}$ to go from -1.4° to 1.4° by our choice of integration boxes for the intensity. The effect of the $\chi - \chi_{hk}$ cutoff is not very important because most of the observed intensity was included in the integration boxes. In contrast, the cutoff on ω due to the substrate blocking the scattering is important, especially for lower h orders.

We assume the mosaic distribution to be an azimuthally symmetric 2D Lorentzian, which has been observed experimentally in this laboratory (manuscript in preparation),

$$P(\alpha) = \frac{N}{\alpha^2 + \alpha_M^2}, \tag{32}$$

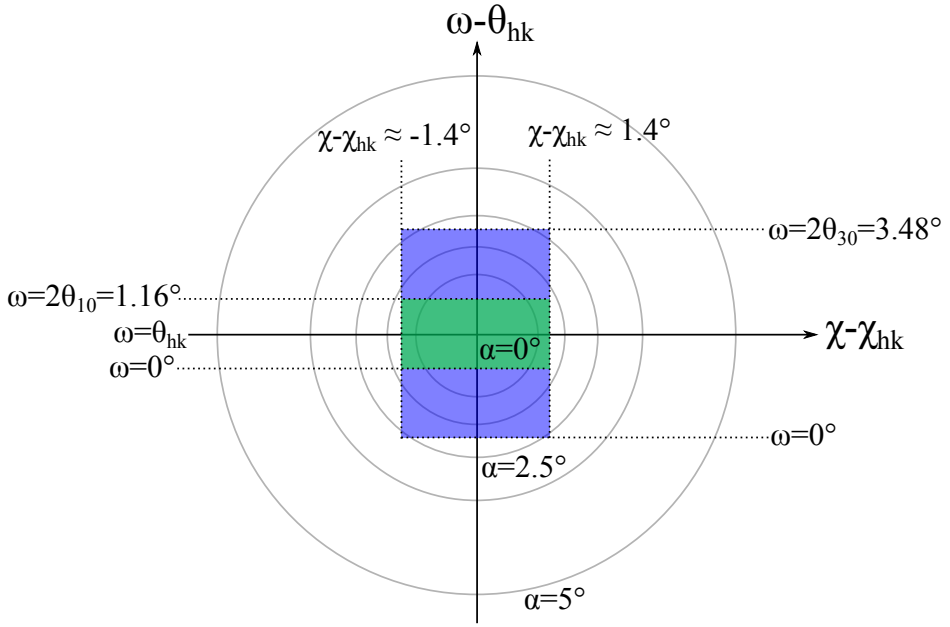

Fig. S8 Contours of a mosaic spread distribution projected on the $\omega\chi$-plane, where $\chi - \chi_{hk}$ is an angle measured from a (h,k) reflection on the detector ($\chi = \pi/2 - \phi$ in Fig. 1) and θ_{hk} is the Bragg angle for the (h,k) reflection. The distribution function is assumed to be a 2D Lorentzian centered at $\alpha = 0$. Domains with $\alpha = 0$ are probed at $\omega = \theta_{hk}$ and $\chi = \chi_{hk}$. Integrated intensity of $(1,k)$ reflections arise from domains in the green shaded area while that of $(3,k)$ reflections are from the blue shaded area, which is three times larger.

where N is a normalization constant and α_M is the half width half maximum of the distribution. N satisfies

$$N = \frac{1}{2\pi}\left(\int_0^{\frac{\pi}{2}} d\alpha \, \frac{\alpha}{\alpha^2 + \alpha_M^2}\right)^{-1}. \tag{33}$$

For small α, Eq. 32 can be approximated in terms of Cartesian coordinates as

$$P(\omega,\chi) \approx \frac{N}{\omega^2 + \chi^2 + \alpha_M^2}. \tag{34}$$

We then consider a two dimensional contour map on the $\omega\chi$ plane, as shown in Fig. S8. Mosaic factor for a reflection with Bragg angle θ_B is given by

$$M = \int_{-\theta_B}^{\theta_B} d\omega \int_{-\chi_0}^{\chi_0} d\chi \, P(\omega,\chi) = \int_{-\theta_B}^{\theta_B} d\omega \int_{-\chi_0}^{\chi_0} d\chi \, \frac{N}{\omega^2 + \chi^2 + \alpha_M^2} \tag{35}$$

After the integration over χ, Eq. (35) is

$$M = 4N \int_0^{\theta_B} \frac{d\omega}{\sqrt{\omega^2 + \alpha_M^2}} \arctan\left(\frac{\chi_0}{\sqrt{\omega^2 + \alpha_M^2}}\right). \tag{36}$$

Eq. (36) is plotted in Fig. S9.

S2.5 Synopsis of Intensity Corrections

Tables S1 and S2 show the values of the corrections obtained from the analysis in the previous three subsections using properties of our samples. The absorption and mosaicity corrections are significant for the lowest orders and their product largely accounts for the smaller intensities previously noted[2] for the lower orders of gel phase oriented samples compared to unoriented MLV samples which do not have these corrections. These two corrections decrease gradually as h increases with small modulations with k. In contrast, the Lorentz correction varies strongly with both h and k although it is the same for the same h/k. The importance of the previous three sections is emphasized by the result that the largest correction for $(1,3)$ is a factor of 367 greater than for the smallest correction for $(1,0)$.

h	k	Absorption	Mosaicity	Lorentz	All
1	-1	1.96	2.63	14.16	73.086
1	0	1.41	2.56	0.11	0.394
1	1	1.79	2.56	12.67	58.027
1	2	1.74	2.53	25.00	110.055
1	3	1.69	2.50	34.12	144.592
2	-2	1.45	2.27	14.19	46.738
2	-1	1.43	2.27	6.97	22.641
2	0	1.19	2.22	0.22	0.577
2	1	1.41	2.22	6.45	20.187
2	2	1.39	2.22	12.51	38.607
2	3	1.39	2.22	18.29	56.444
2	4	1.39	2.22	23.92	73.827
2	5	1.39	2.17	28.76	86.837
2	6	1.37	2.17	33.73	100.446
3	-2	1.30	2.13	9.31	25.723
3	-1	1.30	2.13	4.50	12.436
3	0	1.14	2.13	0.33	0.788
3	1	1.28	2.08	4.35	11.586
3	2	1.28	2.08	8.52	22.766
3	3	1.28	2.08	12.56	33.555
3	4	1.27	2.08	16.42	43.295
3	5	1.27	2.08	20.18	53.212
3	6	1.27	2.08	23.81	62.802
4	-3	1.23	2.04	10.54	26.557
4	-2	1.22	2.04	6.94	17.265
4	-1	1.22	2.04	3.40	8.454
4	0	1.10	2.04	0.44	0.976
4	1	1.22	2.04	3.28	8.153
4	2	1.22	2.04	6.39	15.897
4	3	1.21	2.04	9.50	23.450
4	4	1.20	2.04	12.60	30.981
4	5	1.20	2.04	15.49	38.076
4	6	1.20	2.04	18.35	45.126

Table S1 Correction factors for the raw intensities of the ripple LAXS peaks for thickness of an oriented sample t = 10 μm and mosaic spread α_M = 0.05°.

h	*k*	Absorption	Mosaicity	Lorentz	All
5	-3	1.19	2.00	8.44	20.084
5	-2	1.19	2.00	5.49	13.060
5	-1	1.19	2.00	2.64	6.291
5	0	1.08	2.00	0.54	1.169
5	1	1.19	2.00	2.43	5.774
6	-4	1.16	2.00	9.36	21.778
6	-3	1.16	2.00	6.92	16.094
6	-2	1.16	2.00	4.47	10.389
6	-1	1.16	2.00	2.23	5.193
6	0	1.06	2.00	0.65	1.389
6	1	1.16	2.00	2.24	5.217
6	2	1.16	2.00	4.40	10.208
6	3	1.15	2.00	6.38	14.657
6	4	1.15	2.00	8.40	19.309
7	-4	1.14	1.96	7.94	17.682
7	-3	1.14	1.96	5.86	13.060
7	-2	1.14	1.96	3.82	8.512
7	-1	1.14	1.96	1.86	4.145
7	0	1.05	1.96	0.76	1.569
8	0	1.04	1.96	0.87	1.773
9	-5	1.11	1.96	7.60	16.549
9	-4	1.11	1.96	6.07	13.233
9	-3	1.11	1.96	4.50	9.790
9	-2	1.11	1.96	2.98	6.497
9	-1	1.11	1.96	1.50	3.263
9	0	1.04	1.96	0.98	2.000

Table S2 Corrections for the intensities of the ripple LAXS peaks (continued from Table S1).

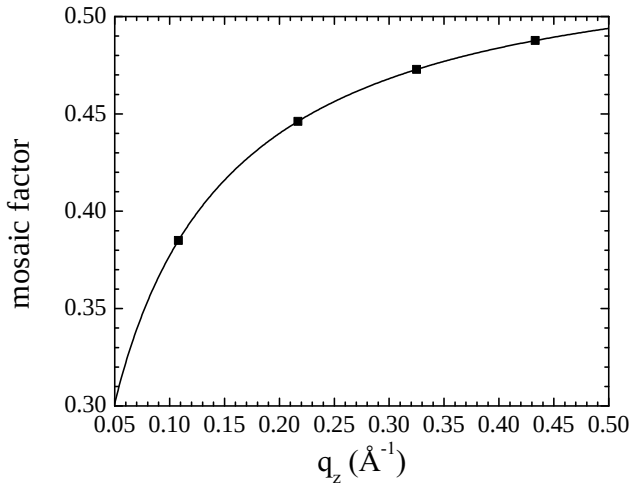

Fig. S9 Mosaic factor given by Eq. (36) as a function of $q_z \approx 4\pi\theta/\lambda$. Values at $q_z = 2\pi h/D$ corresponding to $D = 57.8$ Å are shown as squares. $\alpha_M = 0.05°$ and χ_0=1.4°. Eq. (36) reaches ∼0.54 at $\theta_B = \pi/2$ and $\chi_0 = 1.4°$ and reaches ∼1 at $\theta_B = \pi/2$ and $\chi_0 = \pi/2$ as expected.

S3 Results for $|F_{hk}|$ Form Factors

Tables S3 and S4 list the observed (h,k) reflections and their q_z and q_r values for our best sample shown in Fig. 2. The q_z values for observed peaks were corrected for index of refraction. Column $I_{hk}^{\rm obs}$ is the sum of intensity observed within an integration box centered on the peak with size shown in the box size column. These intensities were multiplied by the total correction factor redisplayed from Table S1, and the square root was taken to obtain unnormalized $|F_{hk}|$. As there is an arbitrary scale factor in the data, the $|F_{hk}|$ shown in Table S3 were then normalized to set $|F_{10}| = 100$.

The σ_I column in table S3 gives uncertainties on $I_{hk}^{\rm obs}$. The largest contribution to σ_I for weak orders was the background scattering, which was assumed to be a constant for each peak and estimated by plotting a swath along a given peak and seeing where the peak tail ended. This was done visually and repeating the process led to differences which determined the estimated σ_I. For some peaks, uncertainty mostly came from the mosaic arc of stronger nearby peaks. For example, the (4, -1) peak was a strong order, but the mosaic arc of its nearby stronger (4, 0) peak overlapped with the (4, -1) peak, giving a relatively large uncertainty

on the (4, -1) peak. While most $k < 0$ peaks were susceptible to mosaic arc, $k > 0$ peaks were not. Therefore, though $k > 0$ peaks were weaker compared to corresponding $k < 0$ peaks, their integrated intensity had smaller σ_I. We assigned a large uncertainty on the (3, 1) peak because it overlapped with the q_z tail of the (3, -1) peak, making separation of (3, 1) and (3, -1) difficult. It was also not clear whether the (3, 1) peak was extinct or not. σ_I for this peak was estimated by placing a box centered at the nominal position of this peak, and it is likely that a fraction of the intensity assigned to (3, -1) in table S3 belongs to (3, 1). The (1, 1) and (1, -1) also overlapped in a similar manner, so their relative σ_I are larger than some of the well separated less intense peaks. Some peaks, such as (1, 2), (4, 3), (6, 2), (9, -1), (9, -3), and all the $(8,k)$ peaks were deemed to be extinct because neighboring peaks had observable intensity. As zero is also an observation, these orders were also included in the table.

To assign uncertainties to the absolute form factors $|F| = \sqrt{I}$ requires propagating σ_I to σ_F. To do this, we estimated the most likely upper bound on each measured intensity $I + \sigma_I$. The most likely upper bound for $|F|$ was determined by $(|F| + \sigma_F)^2 = I + \sigma_I$, which gives σ_F,

$$\sigma_F = |F| \left(-1 + \sqrt{1 + \frac{\sigma_I}{|F|^2}} \right). \tag{37}$$

In the small σ_I/I regime, $\sigma_F = \sigma_I/(2|F|)$. In the large σ_I/I regime, $\sigma_F = \sqrt{\sigma_I}$. For the lower limit, a similar consideration gives the same uncertainty $\sigma_F = \sigma_I/(2|F|)$ for the small σ_I/I. The lower limit in the σ_I/I regime should be zero for the absolute form factors $|F|$. For the form factor F, we take σ_F given by Eq. (37) as an estimated uncertainty. For very weak peaks whose intensity could not be determined but whose nearby peaks were observed, we assigned $|F| = 0$ and $\sigma_F = \sqrt{\sigma_I}$ where σ_I was estimated based on the background scattering intensity at the q value corresponding to those unobserved weak peaks.

Our best oriented sample in Fig. 2 had almost the same D, γ, and only slightly different λ_r as the best data of Wack and Webb[3] from an unoriented sample. Table S5 compares our oriented $\left|F_{hk}^{\text{ori}}\right|$ with the unoriented $\left|F_{hk}^{\text{un}}\right|$. The most obvious comparison is that there are very few unoriented orders, only 18 compared to 60 orders in tables S3 and S4. We could not determine the form factors for the $h = 0$ orders for our oriented sample because of strong attenuation of X-rays at $\omega \approx 0°$. As noted in Sun *et al.*[4], however, inclusion of $h = 0$ orders would not significantly alter the bilayer structure, so these orders were omitted in Table S3. The $k = 5$ and $k = 6$ reflections shown in Table S5 provide higher in-plane resolution in the

h	k	q_z (Å^{-1})	q_r (Å^{-1})	box size (pixels)	I_{hk}^{obs} ($\times 10^3$)	σ_I	correction	$\lvert F_{hk}\rvert$	σ_F	phase factor
1	-1	0.102	-0.043	10 × 7	726.0	63.0	73.086	86.3	3.7	−
1	0	0.109	0.000	10 × 7	180818.0	1759.0	0.394	100.0	0.5	−
1	1	0.114	0.043	10 × 7	228.0	28.0	58.027	43.1	2.6	+
1	2				0.0	1.0	110.055	0.0	3.9	−
1	3	0.128	0.130	10 × 7	3.8	0.2	144.592	8.8	0.2	+
2	-2	0.206	-0.087	10 × 7	49.2	3.5	46.738	18.0	0.6	−
2	-1	0.212	-0.044	10 × 7	1818.0	20.0	22.641	76.0	0.4	−
2	0	0.218	0.000	10 × 7	10200.0	174.0	0.577	28.7	0.2	−
2	1	0.224	0.043	10 × 7	550.0	10.0	20.187	39.5	0.4	+
2	2	0.231	0.086	10 × 7	112.0	3.0	38.607	24.6	0.3	−
2	3	0.237	0.129	10 × 7	27.0	0.2	56.444	14.6	0.1	+
2	4	0.243	0.173	10 × 7	8.2	0.4	73.827	9.2	0.2	−
2	5	0.250	0.214	10 × 7	2.6	0.7	86.837	5.6	0.7	+
2	6	0.256	0.257	10 × 7	1.2	0.2	100.446	4.1	0.3	−
3	-2	0.314	-0.087	15 × 7	305.0	15.0	25.723	33.2	0.8	+
3	-1	0.321	-0.043	15 × 7	1205.0	22.0	12.436	45.9	0.4	+
3	0	0.326	0.000	15 × 7	1566.0	110.0	0.788	13.2	0.5	−
3	1			15 × 7	0.0	31.0	11.586	0.0	7.1	−
3	2	0.339	0.086	15 × 7	32.4	1.6	22.766	10.2	0.2	+
3	3	0.345	0.129	15 × 7	39.1	0.9	33.555	13.6	0.2	−
3	4	0.352	0.172	15 × 7	27.7	0.7	43.295	13.0	0.2	+
3	5	0.358	0.215	15 × 7	12.2	0.3	53.212	9.6	0.1	−
3	6	0.364	0.258	15 × 7	3.5	0.5	62.802	5.6	0.4	+
4	-3	0.417	-0.131	20 × 8	142.0	8.0	26.557	23.0	0.6	−
4	-2	0.423	-0.087	20 × 8	755.4	19.0	17.265	42.8	0.5	−
4	-1	0.429	-0.043	20 × 8	429.6	34.0	8.454	22.6	0.9	−
4	0	0.435	0.000	20 × 8	1917.0	23.0	0.976	16.2	0.1	+
4	1	0.441	0.043	20 × 8	45.3	7.2	8.153	7.2	0.6	−
4	2	0.448	0.085	20 × 8	43.6	2.4	15.897	9.9	0.3	−
4	3			20 × 8	0.0	1.3	23.450	0.0	2.1	+
4	4	0.461	0.173	20 × 8	2.1	0.4	30.981	3.0	0.3	−
4	5	0.467	0.215	20 × 8	3.2	0.3	38.076	4.1	0.2	+
4	6	0.473	0.259	20 × 8	1.0	1.1	45.126	2.5	1.1	−

Table S3 Observed intensity, derived form factor amplitudes, and phase factors for h = 1 to 4 at $D = 57.8$ Å, $\lambda_r = 145$Å, and $\gamma = 98.2°$.

h	k	q_z (Å^{-1})	q_r (Å^{-1})	box size (pixels)	I_{hk}^{obs} ($\times 10^3$)	σ_I	correction	$\lvert F_{hk}\rvert$	σ_F	phase factor
5	-3	0.525	-0.132	25 × 9	86.2	6.8	20.084	15.6	0.6	−
5	-1	0.538	-0.042	25 × 9	63.4	3.4	6.291	7.5	0.2	+
5	0	0.544	0.000	25 × 9	260.0	4.0	1.169	6.5	0.1	+
5	1	0.550	0.040	25 × 9	50.0	2.8	5.774	6.4	0.2	−
6	-4	0.628	-0.175	30 × 10	11.4	0.8	21.778	5.9	0.2	+
6	-3	0.635	-0.131	30 × 10	15.6	0.9	16.094	5.9	0.2	+
6	-2	0.641	-0.085	30 × 10	10.1	1.8	10.389	3.8	0.3	+
6	-1	0.647	0.043	30 × 10	16.3	3.0	5.193	3.4	0.3	−
6	0	0.653	0.000	30 × 10	60.2	4.7	1.389	3.4	0.1	+
6	1	0.659	0.044	30 × 10	20.4	1.5	5.217	3.9	0.1	+
6	2			30 × 10	0.0	0.6	10.208	0.0	0.9	−
6	3	0.672	0.128	30 × 10	5.9	0.3	14.657	3.5	0.1	+
6	4	0.679	0.170	30 × 10	4.2	0.3	19.309	3.4	0.1	−
7	-4	0.737	-0.174	35 × 10	40.0	1.1	17.682	10.0	0.1	−
7	-3	0.743	-0.130	35 × 10	36.0	1.8	13.060	8.1	0.2	−
7	-2	0.749	-0.085	35 × 10	15.0	7.3	8.512	4.2	0.9	+
7	-1	0.755	-0.042	35 × 10	22.0	2.3	4.145	3.6	0.2	+
7	0	0.760	0.000	35 × 10	36.0	1.8	1.569	2.8	0.1	−
8	0				0.0	3.0	1.773	0.0	0.9	+
9	-5	0.951	-0.215	35 × 10	16.0	3.0	16.549	6.1	0.5	−
9	-4	0.957	-0.173	35 × 10	16.9	3.0	13.233	5.6	0.5	−
9	-3			35 × 10	0.0	8.0	9.790	0.0	3.3	+
9	-2	0.969	-0.086	35 × 10	10.0	2.9	6.497	3.0	0.4	+
9	-1			35 × 10	0.0	6.0	3.263	0.0	1.7	−
9	0	0.981	0.000	35 × 10	17.0	10.0	2.000	2.2	0.6	+

Table S4 Observed intensity, derived form factor amplitudes, and phase factors for h = 5 to 9 at $D = 57.8$ Å, $\lambda_r = 145$ Å, and $\gamma = 98.2°$ (continued from Table S3).

oriented data, and the observability of the lamellar orders all the way to $h = 9$ provides three times higher resolution along the z-axis.

As discussed extensively in the previous section, oriented samples require complex corrections, so comparison with the relatively straightforward Lorentz correction from an unoriented sample with similar structure allows us to check our corrections. Although the ratios of the normalized form factors vary from 0.62 to 1.38, there appears to be no sign that our corrections are flawed. We propose a different reason why the ratios deviate so much from unity. In X-ray data from an oriented sample, most peaks were well separated on the two-dimensional CCD, so integrating a peak intensity was usually straightforward. In contrast, intensities from unoriented data are collapsed onto one-dimension and overlap much more, making separation of intensity difficult. Three such pairs of overlapping peaks are highlighted in Table S5. We show a modified $\left|F_{hk}^{\mathrm{un}}\right|$ in Table S5 where we have shifted some intensity from the (1, 0) peak to the (1, -1) peak and some intensity from the (2, 0) peak to the (2, -1) peak. Although there is a remaining discrepancy for the (1, 1) reflection, the modified ratios are generally improved. Of course, even though it makes sense to compare these unoriented and oriented samples, one should not expect perfect agreement, especially as the ripple wavelength differs by 2.3%.

h	k	q (Å^{-1})	unoriented $\lvert F_{hk}^{un}\rvert$	oriented $\lvert F_{hk}^{ori}\rvert$	ratio	modified $\lvert F_{hk}^{un}\rvert$	ratio
1	-1	0.111	60.8	86.3	0.70	83.0	0.96
1	0	0.108	100.0	100.0	1.00	100.0	1.00
1	1	0.123	26.9	43.1	0.62	29.9	0.69
1	2			0.0			
1	3	0.185	7.6	8.8	0.87	8.4	0.96
2	-2	0.224	15.1	18.0	0.84	16.8	0.93
2	-1	0.215	71.2	76.0	0.94	85.1	1.12
2	0	0.217	39.7	28.7	1.38	30.9	1.08
2	1	0.228	33.9	39.5	0.86	37.6	0.95
2	2	0.246	22.7	24.6	0.92	25.2	1.02
2	3	0.271	14.2	14.6	0.97	15.8	1.08
2	4	0.301	7.8	9.2	0.85	8.7	0.94
2	5	0.329		5.6			
2	6			4.1			
3	-2	0.325	29.3	33.2	0.88	32.5	0.98
3	-1	0.322	44.2	45.9	0.96	49.1	1.07
3	0	0.325	12.0	13.2	0.91	13.3	1.01
3	1			0.0			
3	2	0.350	10.5	10.2	1.03	11.7	1.15
3	3	0.370	14.9	13.6	1.10	16.5	1.22
3	4	0.394	10.0	13.0	0.77	11.1	0.86
3	5			9.6			
3	6			5.6			

Table S5 Comparison of form factors $\left|F_{hk}^{\mathrm{un}}\right|$ for the unoriented sample from Wack and Webb[3] and $\left|F_{hk}^{\mathrm{ori}}\right|$ from an oriented sample from this study. The ratio $\left|F_{hk}^{\mathrm{un}}\right| / \left|F_{hk}^{\mathrm{ori}}\right|$ of unoriented to oriented form factors is shown. Three pairs of reflections with very nearly the same q values are shown in color. A modification is shown that partitions the total intensity of unoriented reflections with nearly the same q, as described in the text.

S4 Additional Electron Density Map

The phase factors used to obtain the electron density map in Fig. 4 in the paper are shown in Tables S3 and S4. They were obtained using a model. Different models had the same signs for the phase factors for the strongest reflections with $h < 6$. The second best model, as determined by the sum of the mean square deviations from the measured $|F_{hk}|$, had the same signs. The third best model had opposite signs for all the $h = 6$ reflections. That electron density map is shown next.

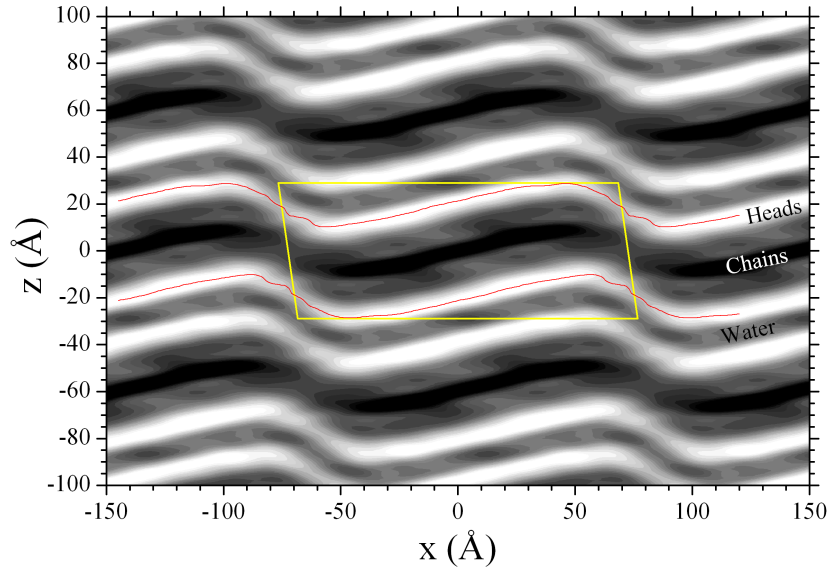

Fig. S10 Two dimensional electron density map calculated using the alternate set of phase factors, in linear grayscale.

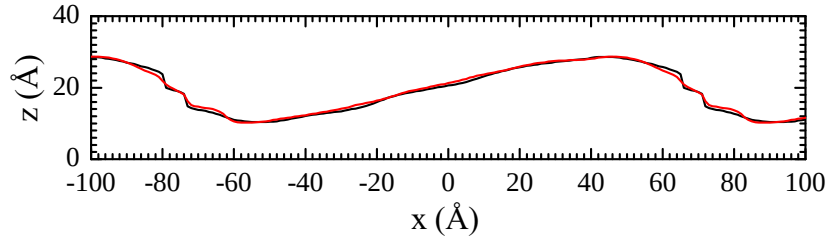

Fig. S11 Comparison of the locus of the maximum electron density for two sets of the phase factors. The black line is from Fig. 4, and the red line is from the alternate set of phase factors (red line in Fig. S10).

S5 Thin Rod Model

To understand the WAXS data we considered models of chain packing. As the prevailing hypothesis is that the major arm of the ripple is like a gel phase, we begin by reviewing gel phase models in the next subsection. We then consider the scattering consequences of tilting these models out of plane by the angle $\xi_M \approx 10.5^\circ$ obtained from the LAXS analysis.

S5.1 Gel Phase Model

The fully hydrated gel phase of DMPC consists of hydrocarbon chains that are basically straight and cooperatively tilted by an angle θ from the bilayer normal[5–8]. This is called the $L_{\beta I}$ phase in which each chain is tilted toward a nearest neighbor chain. At lower hydration the chains tilt differently. We will also focus on the $L_{\beta F}$ phase in this section. The chains will be modeled as thin rods. The basic geometry of the $L_{\beta I}$ and $L_{\beta F}$ phases is shown in Fig. S12. Ref.[7] emphasized that the chains are tilted in the same direction in both monolayers. It also allowed for translational offsets that we will set to zero for simplicity.

The unit cell customarily employed is indicated in Fig. S12. For the $L_{\beta I}$ phase, the chains are tilted along the **b** direction as shown in Fig. S12 and along the **a** direction for the $L_{\beta F}$ phase. It may be noted that chain packing in a plane that is perpendicular to the chains (and therefore not parallel to the bilayer) is nearly hexagonal; if the packing were hexagonal and if the chains had zero tilt, then in Fig. S12, one would have $b = a/\sqrt{3}$, which becomes $b = a/(\sqrt{3}\cos\theta)$ with tilt. The Laue conditions for allowed reflections are

$$q_x = \frac{2\pi m}{a} \tag{38}$$

and

$$q_y = \frac{2\pi n}{b}, \tag{39}$$

where m and n are integers. Eq. 38 and 39 establish the location of possible lines of scattering (Bragg rods). The modulation of the intensity along these rods is derived from the square of the unit cell form factor

$$F(\mathbf{q}) = \int_0^a dx \int_0^b dy \int_{-\frac{L}{2}\cos\theta}^{\frac{L}{2}\cos\theta} dz\, \rho(\mathbf{r}) \exp(i\mathbf{q}\cdot\mathbf{r}). \tag{40}$$

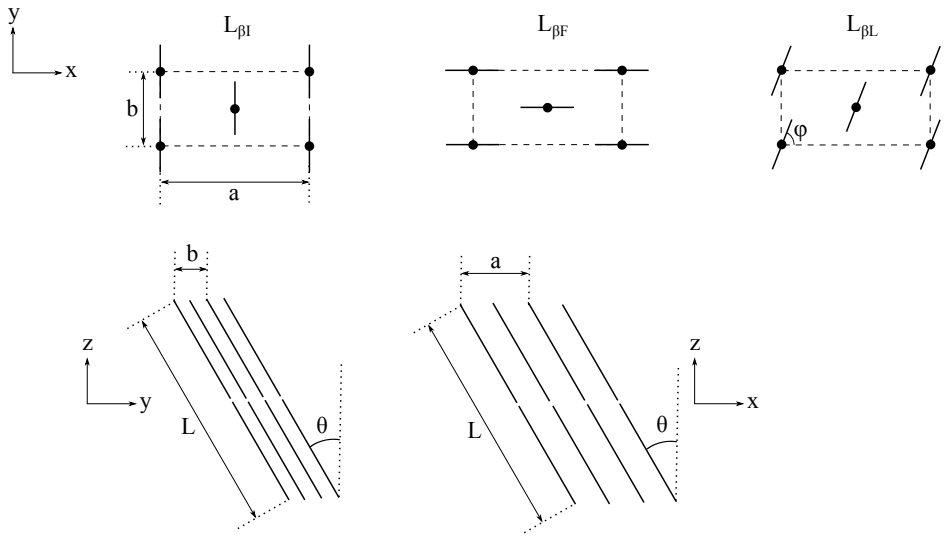

Fig. S12 Lattice and geometry of thin rod model. The chains are represented as solid lines. The unit cell is drawn in the dashed lines. Top views of $L_{\beta I}$, $L_{\beta F}$, and $L_{\beta L}$ phases (top) and side views of $L_{\beta I}$ and $L_{\beta F}$ (bottom) are shown. **a** and **b** are unit cell vectors, and $a > b$. ϕ is an in-plane azimuthal angle. θ is the chain tilt angle with respect to the bilayer normal z. Chains are tilted toward the nearest neighbor in the $L_{\beta I}$ phase with $\phi = \pi/2$. The $L_{\beta I}$ phase is observed in the fully hydrated gel phase of DMPC. In the $L_{\beta F}$ phase, the chains are tilted toward the next nearest neightbor ($\phi = 0$).

Our thin rods are modeled as delta functions

$$\rho(\mathbf{r}) = \delta(x - \alpha z, y - \beta z) + \delta(x - a/2 - \alpha z, y - b/2 - \beta z) \tag{41}$$

where for the general case that the chain tilt is oriented at angle ϕ relative to the x axis

$$\alpha = \tan\theta \cos\phi \tag{42}$$

and

$$\beta = \tan\theta \sin\phi. \tag{43}$$

For the $L_{\beta I}$ phase, $\phi = \pi/2$ and for the $L_{\beta F}$ phase, $\phi = 0$. Continuing with the general ϕ case for awhile, defining $\gamma = \alpha q_x + \beta q_y + q_z$ yields

$$F(\mathbf{q}) = \int_{-\frac{L}{2}\cos\theta}^{\frac{L}{2}\cos\theta} dz\, \rho(\mathbf{r}) e^{i\gamma z} (1 + e^{\frac{q_x a}{2} + \frac{q_y b}{2}}). \tag{44}$$

The phase factor $1+e^{q_x a/2+q_y b/2}$ vanishes unless the sum $m+n$ of the Laue indices (m,n) is even. Only the lowest orders $(\pm 2,0)$ and $(\pm 1,\pm 1)$ have observable intensity. For the simple thin rod model in Eq. 41

$$F(q_z) = \frac{4}{\gamma}\sin\left(\frac{\gamma L\cos\theta}{2}\right) \tag{45}$$

so the intensity $|F(q_z)|^2$ is modulated along each Bragg rod and maximum intensity occurs when $\gamma = 0$ which, upon reversing the convention for the sign of q_z, means that the wide angle peaks are centered at

$$q_z^{mn} = \alpha q_x + \beta q_y = \alpha\frac{2\pi m}{a} + \beta\frac{2\pi n}{b}. \tag{46}$$

For the $L_{\beta I}$ phase with $\phi = \pi/2$, one has

$$0 = q_{z\beta I}^{20} = q_{z\beta I}^{-20} \tag{47}$$

$$\frac{2\pi}{b}\tan\theta = q_{z\beta I}^{11} = q_{z\beta I}^{-11} = -q_{z\beta I}^{1-1} = -q_{z\beta I}^{-1-1} \tag{48}$$

For the $L_{\beta F}$ phase with $\phi = 0$

$$\frac{4\pi}{a}\tan\theta = q_{z\beta F}^{20} = -q_{z\beta F}^{-20} \tag{49}$$

and

$$\frac{2\pi}{a}\tan\theta = q_{z\beta F}^{11} = q_{z\beta F}^{1-1} = -q_{z\beta F}^{-11} = -q_{z\beta F}^{-1-1} \tag{50}$$

One can verify, using these equations and the Laue equations for q_x and q_y that the magnitudes $q^{\pm 2,0}$ and $q^{\pm 1,\pm 1}$ of the total scattering vectors are equal when the packing of the chains is hexagonal in the tilted chain plane.

In q-space the powder averaged gel phase pattern consists of circles in q_x and q_y centered on $q_x = 0 = q_y$ and with the values of q_z given in Eqs. 47–50. The location of observed scattering in lab space $\mathbf{k}$ is obtained using the Ewald sphere, centered at $\mathbf{k} = 0$ with radius $2\pi/\lambda$ and with the $\mathbf{q} = 0$ center of the q-space pattern located at $\mathbf{k} = (0,|\mathbf{k}|,0)$. The q-space pattern is tilted by the angle ω when the sample is tilted relative to the laboratory frame; for grazing incidence, the q_z and k_z axes are parallel and offset by $2\pi/\lambda$ in the k_y beam direction. The direction of scattering for the powder averaged gel phase is given by the laboratory $\mathbf{k}$ values where the q-space pattern intersects the Ewald sphere. Each of the (m,n) rings

generally intersects twice with opposite signs for k_x corresponding to opposite sides of the meridian on the CCD. The only rings that give observable scattering in the gel phase are the $(\pm 2, 0)$ and the $(\pm 1, \pm 1)$ rings. However, some of these six rings may coincide. For the $L_{\beta I}$ phase $(\pm 2, 0)$, $(\pm 1, 1)$ and $(\pm 1, -1)$ are pairwise identical, so there are three primary reflections on each side of the meridian. For the $L_{\beta F}$ phase $(1, \pm 1)$ and $(-1, \pm 1)$ are pairwise identical, so there are four primary peaks on each side of the meridian.

S5.2 Ripple Phase Model

A reasonable hypothesis is that the major arm of the ripple has similar internal structure to a gel phase, with the major difference that the plane of the major arm is tilted relative to the substrate. That suggests that the predicted ripple pattern might be the same as would be obtained by tilting the in-plane powder averaged gel phase. However, this would be a fundamental error because the operations of tilting and in-plane powder averaging do not commute. It is necessary first to tilt the gel phase q-space pattern and then to powder average it about the laboratory k_z axis.

Furthermore, the axis for tilting matters, so it is important to define all angles carefully as shown in Fig. 8. We continue to define the chain tilt angle relative to the bilayer normal by θ. The tilt of the major arm will be defined by a rotation angle ξ about an axis in the (x,y) plane and the angle that this axis makes with the x axis will be defined to be ζ. Starting from the q values obtained for the various gel phases, the proper order of rotations is first to rotate the orientation of the lattice with respect to the lab frame; this involves the standard rotation of the (x,y) plane about the z axis by angle ζ. Then, the gel phase is rotated about the new in-plane x axis. The rotated q value will be denoted $\tilde{q}$ which has components

$$\tilde{q}_z^{mn} = q_z^{mn} \cos\xi + q_x^{mn} \sin\xi \, sin\zeta - q_y^{mn} \sin\xi \cos\zeta, \tag{51}$$

$$\tilde{q}_x^{mn} = q_x^{mn} \cos\zeta + q_y^{mn} \sin\zeta, \tag{52}$$

and

$$\tilde{q}_y^{mn} = q_y^{mn} \cos\xi \cos\zeta - q_x^{mn} \cos\xi \sin\zeta + q_z^{mn} \sin\xi. \tag{53}$$

As there are many domains in each X-ray exposure, the next step powder averages each (m,n) reflection by rotating about the z axis from 0 to 2π. As for the gel phase, the ensuing q space pattern consists of circles parallel to the (x,y) plane with center at $(0,0,q_z^{mn})$. As noted above for the gel phase, this pattern is tilted by ω when the substrate is tilted for our transmission experiments. Intersections

of these circles with the Ewald sphere determines the angle of scattering in the laboratory from which, by standard equations (Sec. S1), the $\mathbf{q}_{mn}$ are determined.

The most pertinent component is $\tilde{q}_z^{mn}$ as this primarily determines how far reflections are from the meridian. As there are many variable angles, let us consider $\tilde{q}_z^{mn}$ for the most pertinent special cases. It is appropriate here to consider only $\omega = 0$ because experimental data with $\omega \neq 0$ are easily converted to this standard orientation. We will focus on four special cases. First, consider the in-plane orientation ζ of the lattice to have either the longer a axis parallel ($\zeta = 0$) or perpendicular ($\zeta = \pi/2$) to the ripple direction. It may be noted that these two special directions allow uniform packing of the unit cells along the finite ripple direction, whereas the edges of the unit cells are ragged at the boundaries of the major arm for other values of ζ. Also, these two directions are symmetrical. However, as the lipid molecules are chiral and as there is likely disorder at the boundaries of the major arm, one cannot eliminate general ζ angles *a priori*. We will also focus on the special orientations of the tilt direction that correspond to the $L_{\beta I}$ gel phase ($\phi = \pi/2$), which we will henceforth call $P_{\beta I}^{\zeta}$ phases, and the $L_{\beta F}$ gel phase ($\phi = 0$), to be called $P_{\beta F}^{\zeta}$ phases, recognizing, of course, that we are only modeling the major arm of the $P_{\beta'}$ ripple phase. It will also be convenient to simplify to hexagonal packing of the hydrocarbon chains as the orthorhombic symmetry breaking that makes $q_{\text{total}}^{20} \neq q_{\text{total}}^{11}$ is small; then, $b = a/(\sqrt{3}\cos\theta)$ for the $P_{\beta I}^{\zeta}$ phases and $b = a\cos\theta/\sqrt{3}$ for the $P_{\beta F}^{\zeta}$ phases. These simplifications allow us to focus on the chain tilt angle θ and the tilt ξ of the major side for four cases of (ϕ, ζ) and the observable orders $(\pm 2, 0)$ and $(\pm 1, \pm 1)$. Table 2 shows the values of q_z^{mn}, all divided by $2\pi/a$.

Importantly, tilting the gel phase to form putative ripple major arms breaks the degeneracy of many of the gel phase rings. Most notably, all the degeneracies are broken in the $P_{\beta I}^{\zeta=\pi/2}$ special case whereas none are broken in $P_{\beta F}^{\zeta=\pi/2}$. The magnitude of the q_z symmetry breaking is typically $(4\pi/a)\sin\xi \approx 0.32$ Å^{-1} for $\xi = 10.5°$. As $\Delta q_z \approx 0.4$Å, broken symmetry Bragg rods would be predicted to overlap considerably. This could blur them into apparently single Bragg rods, but with larger Δq_z than the intrinsic value of each Bragg rod.

	$(\pm 2, 0)$	$(\pm 1, 1)$	$(\pm 1, -1)$
$L_{\beta I}$	0	$\sqrt{3}\sin\theta$	$-\sqrt{3}\sin\theta$
$P_{\beta I}^{\zeta=0}$	0	$\sqrt{3}\sin(\theta-\xi)$	$-\sqrt{3}\sin(\theta-\xi)$
$P_{\beta I}^{\zeta=\pi/2}$	$\pm 2\sin\xi$	$\sqrt{3}\sin\theta\cos\xi \pm \sin\xi$	$-\sqrt{3}\sin\theta\cos\xi \pm \sin\xi$
	$(\pm 2, 0)$	$(1, \pm 1)$	$(-1, \pm 1)$
$L_{\beta F}$	$\pm 2\tan\theta$	$\tan\theta$	$-\tan\theta$
$P_{\beta F}^{\zeta=0}$	$\pm 2\tan\theta\cos\xi$	$\tan\theta\cos\xi \mp \sqrt{3}\sin\xi/\cos\theta$	$-(\tan\theta\cos\xi \mp \sqrt{3}\sin\xi/\cos\theta)$
$P_{\beta F}^{\zeta=\pi/2}$	$\pm 2(\tan\theta\cos\xi + \sin\xi)$	$\tan\theta\cos\xi + \sin\xi$	$-(\tan\theta\cos\xi + \sin\xi)$

Table S6 q_z^{mn} divided by $2\pi/a$. Same as Table 2 in the paper.

S6 WAXS Data Reduction

We estimated the width of the Bragg rod I by fitting the intensity profile in q_r to two Lorentzians as shown in Fig. S13 (left). The fit resulted in the FWHM Δq_r = 0.025 Å^{-1} centered at 1.478 Å^{-1} and Δq_r = 0.140 Å^{-1} centered at 1.464 Å^{-1}. A fit with a single Lorentzian was not very good, and a broader Lorentzian was necessary to produce a reasonable fit.

We also fitted to two Lorentzians the peak profile in q_r at q_z = 0.12 Å^{-1}, which includes both the Bragg rod I and II. The fit was only successful within a limited range in q_r. This could be due to an underlining broad peak like the one shown in Fig. S13 (left). To investigate this possibility, we fitted the same peak profile with three Lorentzians with fixed widths as shown in Fig. S13 (right). Two of the Lorentzians had fixed widths of 0.025 Å^{-1} representing sharp peaks, and the last one had a fixed width of 0.14 Å^{-1} representing a broad peak. Fig. S13 (right) shows an excellent fit obtained over a wide range in q_r, suggesting that the estimated peak widths are not unreasonable. The widths and positions of the observed peaks are summarized in Table 1.

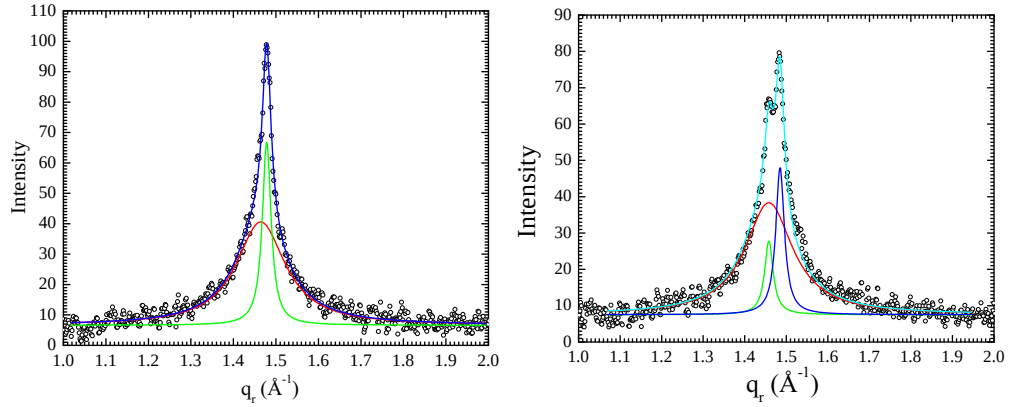

Fig. S13 (left) Peak profile in q_r at q_z = 0.2 Å^{-1} of the GIWAXS pattern shown by open circles in Fig. 3 (left), fitted to the sum of two Lorentzians. The FWHM and center obtained were 0.025 Å^{-1} and 1.478 Å^{-1} (green) and 0.140 Å^{-1} and 1.464 Å^{-1}(red), respectively. The solid blue line is a sum of the two Lorentzian fits. (right) Peak profile in q_r at q_z = 0.12 Å^{-1} fitted to the sum of three Lorentzians. The FWHM were constrained to 0.025 Å^{-1} (blue), 0.025 Å^{-1} (green), and 0.14 Å^{-1} (red). The centers were found to be 1.485 Å^{-1} (blue), 1.458 Å^{-1} (green), and 1.458 Å^{-1} (red). The solid cyan line is a sum of the three Lorentzian fits.

S7 Possible Connection to Simulations

Even though our WAXS data do not support interdigitation in the minor side for our samples, it is interesting that a perturbation of our structure in Fig. 9 could lead to a structure consistent with simulations,[9–11] as shown in the next figure. This suggests that interdigitation in the minor arm might be eliminated by modest modifications in force fields to correspond to our experimental conditions.

Fig. S14 The left sketch repeats the chain packing proposed in Fig. 9 in the text, but with the minor arm in the center. In the right sketch, the left sketch has been separated in the middle of the minor arm and translated so as to provide a gap into which interdigitated chains, shown in magenta, have been inserted.

References

1 http://henke.lbl.gov/optical_constants.

2 S. Guler, D. D. Ghosh, J. Pan, J. C. Mathai, M. L. Zeidel, J. F. Nagle and S. Tristram-Nagle, *Chemistry and Physics of Lipids*, 2009, **160**, 33–44.

3 D. C. Wack and W. W. Webb, *Physical Review A*, 1989, **40**, 2712–2730.

4 W. J. Sun, S. Tristram-Nagle, R. M. Suter and J. F. Nagle, *Proceedings of the National Academy of Sciences*, 1996, **93**, 7008–7012.

5 G. S. Smith, E. B. Sirota, C. R. Safinya and N. A. Clark, *Physical Review Letters*, 1988, **60**, 813–816.

6 S. Tristram-Nagle, R. Zhang, R. M. Suter, C. R. Worthington, W. J. Sun and J. F. Nagle, *Biophysical Journal*, 1993, **64**, 1097–1109.

7 W. J. Sun, R. M. Suter, M. A. Knewtson, C. R. Worthington, S. Tristram-Nagle, R. Zhang and J. F. Nagle, *Physical Review E*, 1994, **49**, 4665–4676.

8 S. Tristram-Nagle, Y. Liu, J. Legleiter and J. F. Nagle, *Biophysical Journal*, 2002, **83**, 3324 – 3335.

9 A. H. de Vries, S. Yefimov, A. E. Mark and S. J. Marrink, *Proceedings of the National Academy of Sciences*, 2005, **102**, 5392–5396.

10 A. Debnath, K. G. Ayappa, V. Kumaran and P. K. Maiti, *The Journal of Physical Chemistry B*, 2009, **113**, 10660–10668.

11 O. Lenz and F. Schmid, *Physical Review Letters*, 2007, **98**, 058104.